Analysis of Electromagnetic Force Ripple in a Bearingless Synchronous Reluctance Motor

Victor Mukherjee[1,3], Paavo Rasilo[2], Floran Martin[1] and Anouar Belahcen[1,4], *Senior Member, IEEE*

[1] Department of Electrical Engineering and Automation, Aalto University, Espoo 02150, Finland
[2] Unit of Electrical Engineering, Tampere University, Tampere 33720, Finland
[3] Technology Center, ABB Motors and Generators, Helsinki 00380, Finland
[4] Department of Electrical Power Engineering and Mechatronics, Tallinn University of Technology, Tallinn 19086, Estonia.

A bearingless machine should be designed to maximize the average and to minimize the ripple in the electromagnetic torque and levitating force. In a bearingless synchronous reluctance machine (BSynRM), the complex rotor design and the levitation winding create a rich spatial and temporal spectrum of the magnetic flux density in the airgap, which affects both the torque and force ripple. In this paper, a novel method is introduced to compute the electromagnetic forces from the spatial harmonics of the airgap flux density. A new indexing method is introduced to classify the spatial harmonic wavenumbers and temporal harmonic frequencies of the flux density in the electromagnetic force. The proposed model enables the understanding of the spatial harmonic footprint on the temporal frequencies of the electromagnetic force ripple. The study is carried out through finite element simulations, which are verified by prototype measurements.

Index Terms— **Bearingless Machine, Electromagnetic Forces, Flux Barriers, Harmonics, Levitation.**

I. Introduction

B EARINGLESS synchronous reluctance motors (BSynRM) offer an integrated combination of a synchronous reluctance motor and active magnetic bearing (AMB) in one common unit. The operation of bearingless motors is based on the interaction between the magnetomotive forces generated by the main winding, an additional winding and, in case of a permanent magnet machine, the magnets [1] - [4]. The main winding is designed to produce the airgap magnetic flux density required for producing the desired torque. The additional winding produces a magnetomotive force, which interacts with the magnetomotive force produced by the main winding. Fig 1 shows that in a certain part of the airgap like region 2, the 4 pole flux and 2 pole flux add to each other, whereas, in some other part of the airgap like region 4, they oppose each other. Therefore, the resultant flux distribution in the airgap under different pole becomes uneven [5]. As a result, the Maxwell stress tensor is also unevenly distributed under each pole which generates an unbalanced magnetic pull, i.e. a net electromagnetic force on the rotor. By controlling this force, the rotor can be levitated. The electromagnetic force acting on the rotor can be considered a combination of two perpendicular components; one opposing the gravity (y-component) and one perpendicular to the gravity (x-component), as shown in Fig. 1. The shaft is considered perfectly horizontal (z-direction).

The electromagnetic forces have different temporal harmonic components arising from the spatial complexity of the stator and the rotor. Thus, the four important design considerations of a bearingless motor are minimizing the torque ripple and force ripple and maximizing the mean torque and levitation force acting on the rotor. In [6], a novel control strategy has been proposed to solve the torque ripple and force ripple problem in a bearingless switched reluctance motor. In [7], a semi-analytical model is presented for a 2-pole bearingless permanent magnet synchronous motor (BPMSM) in order to determine the harmonic components of the airgap flux density. In [8], the spatial harmonics of a BPMSM are investigated and a detailed force ripple model is presented.
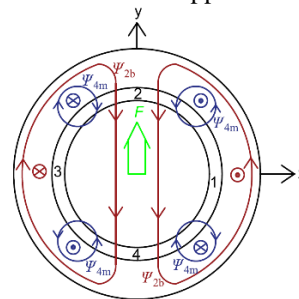

Fig. 1. The main winding flux (blue colour) and additional winding flux (red colour) act in the same direction in the upper part of the airgap (making flux density higher) and in opposite direction in the lower part (making flux density lower), which produces the electromagnetic force denoted by the arrow (green colour).

In [9] and [10], 2D harmonic force models are presented to identify the electromagnetic force ripple components of an eccentric motor to analyse the vibrations of the motor. However, these methods are based on the 2D Fourier analysis of the airgap flux density to understand the spatial and temporal force spectrum. In fact, the spatial harmonic information can be obtained from the 1D Fourier analysis of the airgap flux density at each time step. In this paper, one

quasi-static magnetic flux density distribution is computed in the airgap, from which the spatial harmonics are computed. The time variation of each spatial harmonic can be utilised to develop a model that explains the impact of the airgap spatial harmonics on the force temporal spectrum. In this way, individual force harmonics can be computed faster, enabling a better understanding to control any individual harmonics if required.

This paper has two main goals as given below:

a. Proposing a method to compute the electromagnetic forces from the 1D Fourier analysis of the airgap flux density.

b. Analysing the electromagnetic force harmonics in the spatial and temporal spectrum by proposing a novel indexing technique.

The main benefit of the method is that it enables a comprehensive idea on which pair of spatial harmonics produce which temporal harmonic of the forces. The proposed method of calculating the electromagnetic force is compared with the already established Coulomb's method, which is based on the virtual work principle [11]. The finite element (FE) computation results are validated with measurements on a BSynRM prototype at no-load condition.

The paper is organised as follows: in Section II, the harmonic decomposition method for the force computation is presented and the related spatial harmonic indices are defined. In Section III, the FE method used to compute the flux density harmonic is presented. Section IV presents the validation of the presented results at different levels. Section IV.A presents a validation of the harmonic decomposition method by comparing its results to those obtained from the virtual work principle. Section IV.B presents the experimental validation and related analysis. In addition, the measurement setup is described, the results from two different force-measuring systems are shown, and their comparison with the numerical analysis is presented. Finally, Section V concludes the paper and discusses the relevance of the work and foreseen consequences.

II. HARMONIC DECOMPOSITION MODEL FOR FORCE COMPUTATION

A. Computation of Force

The Fourier decomposition for the angular (θ) dependency of the flux density $\boldsymbol{B}$ in the air gap at airgap radius r in radial and tangential coordinates at any given time t can be written as,

$$\boldsymbol{B}(t,r,\theta) = B_{\text{rad}}(t,r,\theta)\boldsymbol{u}_{\text{rad}}(t,\theta) + B_{\text{tan}}(t,r,\theta)\boldsymbol{u}_{\text{tan}}(t,\theta) \quad (1)$$

where the radial and tangential component of $\boldsymbol{B}$ i.e. B_{rad} and B_{tan} are given as,

$$B_{\text{rad}}(t,r,\theta) = \sum_{i=1}^{\infty} B_{\text{rad},i}(t,r)\cos\left(i\theta + \phi_{\text{rad},i}(r,t)\right) \quad (2)$$
$$B_{\text{tan}}(t,r,\theta) = \sum_{i=1}^{\infty} B_{\text{tan},i}(t,r)\cos\left(i\theta + \phi_{\text{tan},i}(r,t)\right)$$

$B_{\text{rad},i}$ and $B_{\text{tan},i}$ are the radial and tangential components of the ith spatial air-gap magnetic flux density harmonics and $\phi_{\text{rad},i}$ and $\phi_{\text{tan},i}$ are their corresponding phase angles. The unit vectors $\boldsymbol{u}_{\text{rad}}$ and $\boldsymbol{u}_{\text{tan}}$ shown in (1) are given as,

$$\begin{aligned} \boldsymbol{u}_{\text{rad}}(\theta) &= \boldsymbol{u}_{\text{x}}\cos\theta + \boldsymbol{u}_{\text{y}}\sin\theta \\ \boldsymbol{u}_{\text{tan}}(\theta) &= -\boldsymbol{u}_{\text{x}}\sin\theta + \boldsymbol{u}_{\text{x}}\cos\theta \end{aligned} \quad . \quad (3)$$

where $\boldsymbol{u}_{\text{x}}$ and $\boldsymbol{u}_{\text{y}}$ are the unit vectors in the x and y direction. It is worth mentioning that the levitation winding and eccentricity may cause harmonics of order $i < p$, where p is the pole pair number of the main winding. From now on the t, r and θ-dependencies of the quantities are not denoted. The electromagnetic force is calculated from the Maxwell stress as a surface integral around the rotor, assuming a constant radius of integration r (from the centre point of the rotor), which in the 2-D case is reduced into an integral along a circular path around the rotor given as,

$$\begin{aligned} \boldsymbol{F} &= \frac{1}{\mu_0}\oint_S\left((\boldsymbol{B}\cdot\boldsymbol{n})\boldsymbol{B} - \frac{1}{2}|\boldsymbol{B}|^2\boldsymbol{n}\right)dS \\ &= \frac{l}{\mu_0}r\int_0^{2\pi}\left((\boldsymbol{B}\cdot\boldsymbol{n})\boldsymbol{B} - \frac{1}{2}|\boldsymbol{B}|^2\boldsymbol{n}\right)d\theta \end{aligned} \quad (4)$$

where μ_0 is the permeability of the vacuum, S is the surface for integration, and the normal vector $\boldsymbol{n} = \boldsymbol{u}_{\text{rad}}$. Replacing (3) in (4) and further simplification gives,

$$\begin{aligned} \boldsymbol{F} &= \frac{l}{\mu_0}r\int_0^{2\pi}\Big(B_{\text{rad}}B_{\text{tan}}\left(-\boldsymbol{u}_{\text{x}}\sin\theta + \boldsymbol{u}_{\text{y}}\cos\theta\right) \\ &+ \frac{1}{2}\left(B_{\text{rad}}^2 - B_{\text{tan}}^2\right)\left(\boldsymbol{u}_{\text{x}}\cos\theta + \boldsymbol{u}_{\text{y}}\sin\theta\right)\Big)d\theta \end{aligned} \quad . \quad (5)$$

The force components in the x and y direction can be written as a summation of all the individual flux density harmonics of its radial and tangential components. As an example, the force component for the x-direction is presented by

$$\begin{aligned} F_{\text{x}} &= \frac{l}{2\mu_0}r\sum_{i=1}^{\infty}\sum_{j=1}^{\infty}\int_0^{2\pi}\Big(B_{\text{rad},i}B_{\text{rad},j}\cos\left(i\theta + \phi_{\text{rad},i}\right) \\ &\cos\left(j\theta + \phi_{\text{rad},j}\right)\cos\theta - B_{\text{tan},i}B_{\text{tan},j}\cos\left(i\theta + \phi_{\text{tan},i}\right) \\ &\cos\left(j\theta + \phi_{\text{tan},j}\right)\cos\theta - 2B_{\text{rad},i}B_{\text{tan},j}\cos\left(i\theta + \phi_{\text{rad},i}\right) \\ &\cos\left(j\theta + \phi_{\text{tan},j}\right)\sin\theta\Big)d\theta \end{aligned} \quad (6)$$

where any two spatial harmonics are represented as i and j. The length of the machine, rotor outer radius, stator inner radius and the radial coordinate in the airgap are represented by l, r_{r}, r_{s} and r respectively. Now, using Arkkio's method [12] to average the Maxwell stress tensor integration over the whole airgap, (6) can be written as,

$$\begin{aligned} F_{\text{x}} &= \frac{l}{2\mu_0(r_{\text{s}} - r_{\text{r}})}\int_{r_{\text{r}}}^{r_{\text{s}}}r\sum_{i=1}^{\infty}\sum_{j=1}^{\infty}\int_0^{2\pi}\Big(B_{\text{rad},i}B_{\text{rad},j}\cos\left(i\theta + \phi_{\text{rad},i}\right) \\ &\cos\left(j\theta + \phi_{\text{rad},j}\right)\cos\theta - B_{\text{tan},i}B_{\text{tan},j}\cos\left(i\theta + \phi_{\text{tan},i}\right) \\ &\cos\left(j\theta + \phi_{\text{tan},j}\right)\cos\theta - 2B_{\text{rad},i}B_{\text{tan},j}\cos\left(i\theta + \phi_{\text{rad},i}\right) \\ &\cos\left(j\theta + \phi_{\text{tan},j}\right)\sin\theta\Big)d\theta dr \end{aligned} \quad (7)$$

The integration can give nonzero value only when i-j+1, and i-j-1 is zero. So, replacing $j = i\pm1$ and simplifying (7), each individual force harmonic in the x-direction, $F_{x,i}$ can be expressed as,

$$F_{x,i} = \frac{\pi rl}{4\mu_0 \left(r_s - r_r\right)} \int_{r_r}^{r_s} \left(B_{rad,i} B_{rad,i\pm1} \cos(\phi_{rad,i} - \phi_{rad,i\pm1})\right.$$
$$- B_{tan,i} B_{tan,i\pm1} \cos(\phi_{tan,i} - \phi_{tan,i\pm1})$$
$$\left.\mp 2B_{rad,i} B_{tan,i\pm1} \sin(\phi_{rad,i} - \phi_{tan,i\pm1})\right) dr \quad (8)$$

Similar methods can be applied for the y-direction, and the force harmonics $F_{y,i}$ can be expressed as,

$$F_{y,i} = \frac{\pi rl}{4\mu_0 \left(r_s - r_r\right)} \int_{r_r}^{r_s} \left(\pm B_{rad,i} B_{rad,i\pm1} \sin(\phi_{rad,i} - \phi_{rad,i\pm1})\right.$$
$$\mp B_{tan,i} B_{tan,i\pm1} \sin(\phi_{tan,i} - \phi_{tan,i\pm1})$$
$$\left.+ 2B_{rad,i} B_{tan,i\pm1} \cos(\phi_{rad,i} - \phi_{tan,i\pm1})\right) dr \quad (9)$$

The total force can be calculated as a sum of all the combinations of the forces coming from different spatial harmonics. The temporal spectrum of the force in a BSynRM can be easily analysed from each spatial harmonic of the flux density after computing each $F_{y,i}$ over time. For example, the levitation force F_y and the disturbance force F_x can be calculated as,

$$F_y(t) = \sum_{i=1}^{\infty} F_{y,i}(t) \ , \ F_x(t) = \sum_{i=1}^{\infty} F_{x,i}(t) \quad (10)$$

It is worth noting that $B_{rad,1}$, $B_{rad,2}$, $B_{tan,1}$ and $B_{tan,2}$ correspond to the radial and tangential fundamental harmonics created by the additional winding and main winding respectively for a non-eccentric rotor. So, this is one particular case where $i = 1$, and $j = i+1 = 2$. In this case, $B_{rad,1}$, $B_{rad,2}$, $B_{tan,1}$ and $B_{tan,2}$ represent $B_{rad,i}$, $B_{rad,j}$, $B_{tan,i}$ and $B_{tan,j}$. These flux density harmonics along with the 3rd harmonic component produced by the additional winding leads to the main levitation force production. The 3rd harmonic in the flux density appears due to the rotor anisotropy with respect to the additional winding. In the studied machine, the rotor is running at half of the additional winding frequency. A detailed analysis of this operational condition is presented by the authors in [14]. Equation (8) and (9) gives a good understanding of the electromagnetic force harmonics based on the spatial flux density spectrum. To mitigate the electromagnetic force ripple, individual force harmonics can be compensated using current injection, which can be decided based on the spatial flux density spectrum. However, in this paper, we focus primarily on the force harmonic characteristics.

B. Spatial Harmonic Indices

To understand which combination of the flux density spatial harmonics produces which force harmonic in the temporal spectrum, a novel harmonic indexing technique is proposed in this paper. A force is produced by any two flux density spatial harmonics when their harmonic orders i and j differ by one.

The harmonic combination of i and j is represented together to form what we call spatial harmonic indices (*SHI*). The primary motivation to propose this indexing method is to merge the two indices i and j to a single meaningful index which can help to understand the force temporal harmonics and explain their origin. The *SHI* is defined as,

$$SHI = i + j - 2, \ \text{when} \ j - i = 1$$
$$SHI = i + j - 1, \ \text{when} \ i - j = 1 \quad (11)$$

The $|j$-$i|= 1$ in the condition of (11) comes from the requirement of force production. An example of computing the *SHI* is given in Table I. The individual spatial harmonics can be traced back from the *SHI* using the following method:

$$\text{and} \quad i = \frac{SHI\text{-}2}{2} + 2; \ \ j = \frac{SHI\text{-}2}{2} + 1, \text{when } SHI \text{ is even}$$
$$i = \frac{SHI\text{-}1}{2} + 1; \ \ j = \frac{SHI\text{-}1}{2} + 2, \text{when } SHI \text{ is odd} \quad (12)$$

Equation (11) is an example of a bijective mapping of a pair of indices to a single index, $(i, j) \longrightarrow SHI$, under the conditions that $|j$-$i|= 1$. Equation (12) proves that the mapping is unique.

To obtain the necessary harmonics of the magnetic flux density in the air gap, different methods for magnetic field analysis can be utilised. In our study, we use the finite element method, where the field equations are coupled with the windings' circuit equations. This methodology, with two sets of windings, is explained in the next section.

TABLE I
SPATIAL HARMONIC INDICES

Harmonic component (i)	Harmonic component (j)	Spatial harmonic indices
1	2	1
2	1	2
2	3	3
3	2	4
..	..	..
33	34	65
34	33	66
34	35	67
35	34	68

III. FINITE ELEMENT METHOD

The parameters of the BSynRM under consideration are given in Table II. The stator and rotor core are made of iron lamination and has been modelled with non-linear B-H characteristics in the FE analysis as shown in Fig. 2. The mesh, the flux density distribution at rated torque and levitation force production, where both winding sets are supplied with sinusoidal voltage and the winding distribution of the prototype motor are shown in Fig. 3 (a), (b) and (c) respectively. The flux density is computed after solving a quasi-static magnetic problem [12], [13]. Fig. 3 shows that the flux density is higher in the positive y-direction than in the negative y-direction. Therefore, an electromagnetic force is
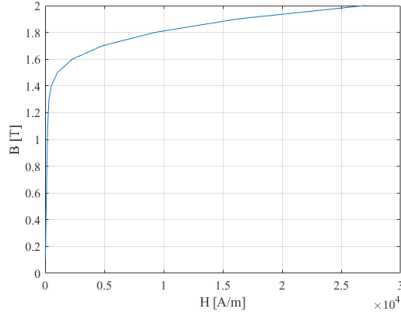
produced in the positive y-direction [15].

Fig. 2. B-H characteristics of the stator and rotor lamination.
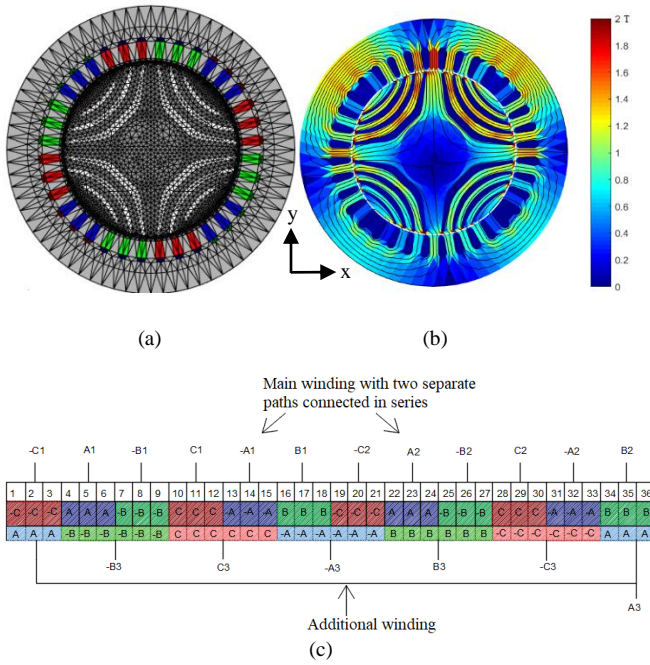

(a)   (b)

(c)

Fig. 3. (a) Mesh of the 2D cross-section of the prototyped motor, (b) computed magnetic flux density of the motor during rated load and levitation force production state, and (c) winding distribution of the two windings in 36 slots, where each slot is numbered in the first row.

A 2D time-stepping FE method is used to determine the harmonics of the airgap flux density and the electromagnetic forces since the FE model is considered as a high-fidelity model. It is good to mention that though the presented harmonic decomposition method is implemented with the FE method, the force harmonic decomposition method can be applied also in other methods like analytical or semi-analytical models, which can provide the magnetic flux density distribution in the airgap of the machine.

In the time-stepping FE method, the model is supplied with current sources during the force ripple analysis so that we can provide a sinusoidal current distribution in both windings. However, to be able to validate the FE model with experiments, the time-stepping FE model is voltage-supplied as the prototype is also supplied with sinusoidal voltages for both windings. From the computational point of view, it is necessary to couple the circuit equation of main and additional

windings in the field equation. In this case, in the FE analysis, the phase currents are solved in the system of equations together with the vector potential given by:

$$
\begin{pmatrix} S(a,\alpha_r) & -(KD_m)^T & -(KD_a)^T \\ 0 & R_m KK^T & 0 \\ 0 & 0 & R_a KK^T \end{pmatrix} \begin{bmatrix} a \\ i_m \\ i_a \end{bmatrix} +
$$
$$
\begin{pmatrix} T & 0 & 0 \\ lKD_m & 0 & 0 \\ lKD_a & 0 & 0 \end{pmatrix} \frac{d}{dt} \begin{bmatrix} a \\ i_m \\ i_a \end{bmatrix} = \begin{bmatrix} 0 \\ Qv_m \\ Qv_a \end{bmatrix}
$$
(13)

where a represents the nodal values of the magnetic vector potential, $S(a,\alpha_r)$ is the magnetic stiffness matrix which depends on the solution and rotor angle α_r. The matrices D map the x- and y-components of the main winding (m) and additional winding (a) current space vectors i into sources of the magnetostatic FE problem. The superscript T stands for matrix transposing operator. v_m and v_a are the terminal voltages of the main and additional windings, T is the damping matrix for the eddy currents in the conducting regions, K, and Q are related to the connection of the stator winding, R_m and R_a are the resistance of the main and additional winding respectively, and l is the length of the machine. Only two independent current variables are solved in the star connection for the main and additional windings separately. To verify the proposed force decomposition model, the already established Coulomb's method is used which is based on the virtual work principle [11] as,

$$
F_{x,y} = \frac{l}{\mu_0} \sum_{e=1}^{N_{eag}} \int_{\Omega_e} \left[-B^T G^{-1} \frac{\partial G}{\partial x, y} B + \frac{1}{2} B^2 |G|^{-1} \frac{\partial |G|}{\partial x, y} \right] d\Omega \quad (14)
$$

where N_{eag} is the total number of elements in the integration band and G is the Jacobian matrix which performs the isoparametric mapping between the local coordinates and the global coordinates of each element in the integration band.

TABLE II
MACHINE DESIGN PARAMETERS

Parameters	Values
Number of poles	4
Number of stator slots	36
Number of phases	3
Length of the motor	195 mm
Outer diameter of the stator core	235 mm
Inner diameter of the stator core	145 mm
Outer diameter of the rotor core	143 mm
Shaft diameter	60 mm
Frequency of supply	50 Hz
Ratio of area of main and additional winding in a slot	4:1
Number of conductors in one slot for main winding	16
Number of conductors in one slot for additional winding	14
Rated power	4.7 kW
Rated levitation force	860 N

IV. VALIDATION

A. Numerical Validation

The simulated radial flux density spectrum at rated torque without and with levitation is presented in Fig. 4, excluding the 50 Hz temporal frequency. The flux density spectrum only at 50 Hz temporal frequency is plotted separately in Fig. 5. The two figures are provided separately for the clarity of representation. It can be seen from Fig. 4 and Fig. 5, that additional harmonic components arise in the magnetic flux density due to the levitation. The slot harmonic components that are visible in the 35th and 37th harmonics have a significant component at higher temporal frequencies like 925 Hz and 975 Hz as presented in Fig. 4. The 5th spatial harmonic has a significant component (0.1 T) at 150 Hz, which is shown with an arrow separately.
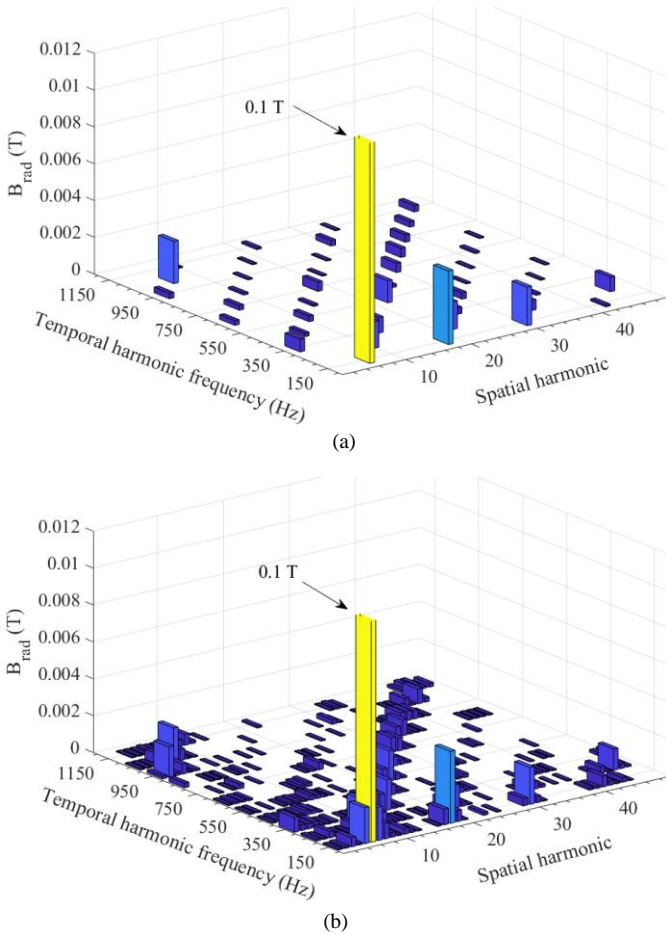

(a)

(b)

Fig. 4. Harmonic spectrum of radial flux density at rated torque (a) without levitation and (b) with levitation.

The 38th spatial harmonic is more visible in the 50 Hz spectrum as shown in Fig. 5. It is worth mentioning that the 37th and 38th harmonics are the "slot number + pole pair" harmonics which are produced mainly by the interaction of the slot with the additional winding and the main winding respectively.

The force computed with both the presented harmonic method and the Coulomb method at the rated operation point is presented in Fig. 6. It can be seen from Fig. 6, that the

proposed harmonic method and the Coulomb's method provide similar results on force computation. The error norm between the two methods is just 0.0083. Using the *SHI* as defined in (11), the 2D harmonic spectrum for the electromagnetic forces in the disturbance direction (x-axis) and in the levitation direction (y-axis) is presented in Fig. 7. Equation (8) and (9) are used to compute each force harmonic indexed with a specific *SHI*. Next, each *SHI* indexed force harmonic is traced after the time-stepping simulation to get its specific temporal spectrum. It should be understood that the force as a global quantity does not have a spatial distribution. However, the definition of the *SHI* makes it possible to plot this 2D spectrum, which in turn makes it possible to trace back to the flux density spectrum. Fig. 6 and Fig. 7 together shows that the *SHI* has uniquely mapped the force harmonics as all the individual force harmonic from Fig. 7 summed up to the correct force expression in the time domain as presented in Fig. 6.
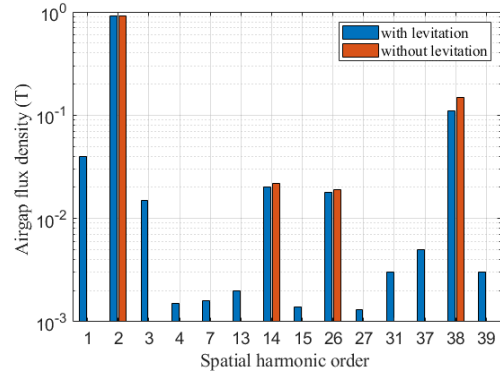

Fig. 5. Spatial harmonic spectrum of radial flux density at rated torque without and with levitation at 50 Hz temporal harmonic.
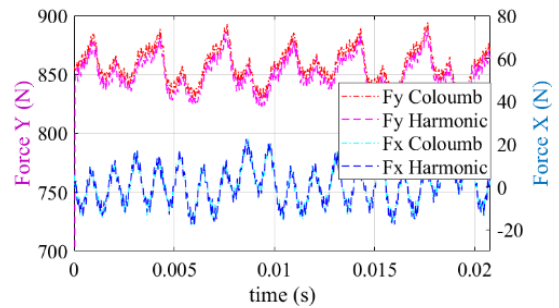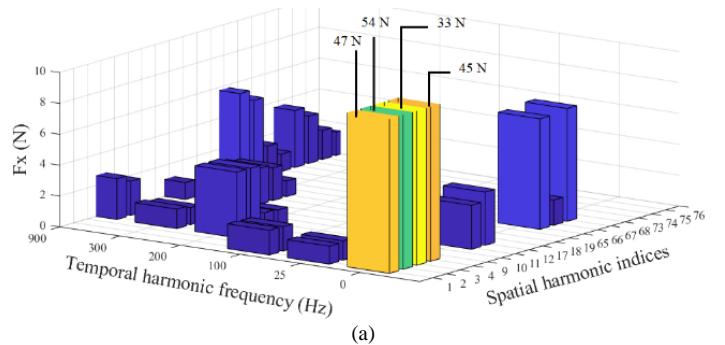

Fig. 6. Comparison of the electromagnetic forces at rated torque and levitation computed with the harmonic method and the coulomb method.
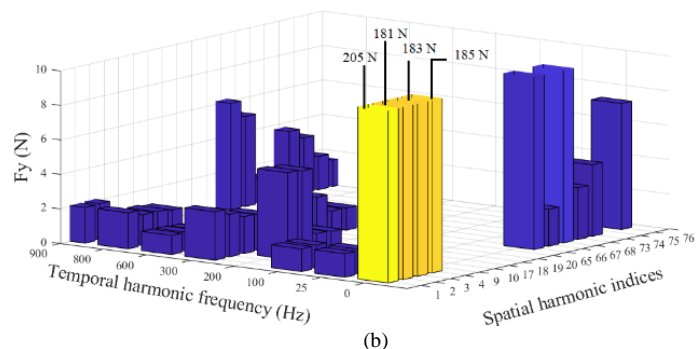

(a)

(b)

Fig. 7. Simulated 2D spectral analysis of the electromagnetic forces in (a) x direction and (b) y direction. Different colours are used to show the different amplitudes of force harmonics distinctively. The spatial harmonics combination for the corresponding *SHI* (1,2,3,4) of yellow, green and brown bars can be found in Table I.

It can be seen from Fig. 7, that the influence of the lower order harmonics in the flux density spectrum is very important, as they generate significant harmonics, nearly 5% ripple, in the temporal spectrum. The presented model can identify the flux density harmonics responsible for the lower order temporal harmonics in the force spectrum. These low order force harmonics are the main reason for the rotor displacement and its misalignment with the stator centre at the levitated state. It is worth mentioning that the forces at 0 Hz temporal frequency represent the net DC forces in each direction.

B. Experimental Validation

1) Description of Setup

A prototype of the BSynRM is constructed in the laboratory and equipped with additional sensors. The position sensors are placed horizontally and vertically near the shaft from both ends. Moreover, each slot is equipped with a search coil with 5 turns. The stator and the rotor of the prototype can be seen in Fig. 8. For practical reasons, the shaft is supported by additional active magnetic bearings (AMB), which are also used to measure the forces as explained below.
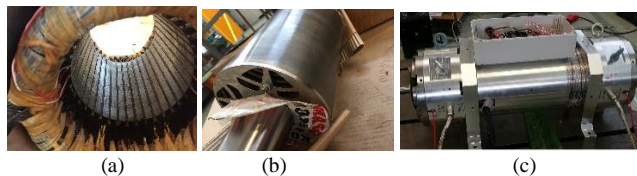

| (a) | (b) | (c) |

Fig. 8. (a) Stator, (b) rotor and (c) prototype machine with the 2 AMBs.

The main idea of the measurement setup is to avoid any external influence on the machine system that can incur additional harmonics. Hence, no frequency converter has been used to levitate the machine or to start the synchronous reluctance machine. The measurement setup is built keeping in focus that the main and additional winding need to be supplied with sinusoidal voltage and similar frequency. To achieve this objective, sinusoidal voltages are fed to both windings by a synchronous generator whose speed can be controlled. The BSynRM is first manually synchronized at low speed using a small motor and then the frequency is increased in a ramp until the rated speed is reached. The main winding is directly connected to a synchronous generator and the voltage is varied through the synchronous generator. For the additional winding, a transformer is used to step down the voltage from the synchronous generator, and the current is further varied using a resistor. In this way, the same frequency is fed to both windings. A schematic representation of the supply to the machine is provided in Fig. 9.

2) Measurement with Search Coil

It can be well understood that the mass inertia of the rotor filters much of the effect of rotor displacements which is caused by the AMB control. It is worth remembering, that the displacement of the rotor induces voltage in the winding. Therefore, if the induced voltage is measured using a search coil, the effect of AMB control can be reduced. This is a primary motivation of using the search coil for the force measurement.
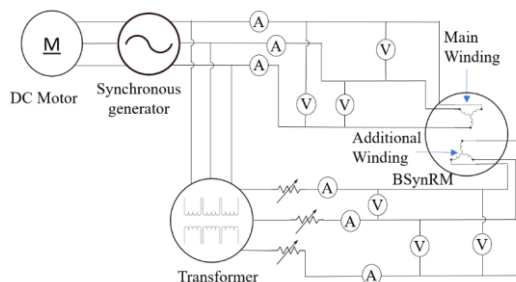

Fig. 9. Schematic representation of the supply to the machine.

The voltages of the search coils, which are put in each slot of the machine are measured with respect to time. The data of the 36 input channels from the 36 slots are captured by the OPAL-RT real-time simulator using 3 analog input ports each having the capacity for receiving 16 input signals. A customized FPGA and CPU model has been built in the OPAL-RT system to access the 36 signals. The voltage waveforms from the slots are time-integrated to calculate the flux in the search coils. After approximating the fringing flux that does not enter in the airgap from the slot, the spatial distribution of the flux density can be approximated in the airgap. In this case, 15 % leakage has been considered between the slots and the airgap. This leakage is estimated based on the FE simulations. The airgap flux density achieved in the aforementioned way is called a measured flux density in this section. The measured and simulated (FE) airgap flux density spatial harmonics, at a given time instant, when the additional winding terminal voltage is kept at 57 V and main winding voltage of 225 V are shown in Fig. 10. In Fig. 10, the odd harmonics result from the additional winding, which is a 1 pole pair winding, whereas, all the even harmonics result from the 2 pole pair main winding and 1 pole pair additional winding. So, all the even harmonics have contributions from both the main and additional winding.

The electromagnetic force is then computed from the flux density in the tooth using the Maxwell stress tensor [12]. All the flux density has been considered as a radial component, and the tangential component of the flux density is neglected as the machine is operated at no-load condition. The total electromagnetic force is obtained as

$$F = \frac{rl\pi}{\mu_0 Q} \sum_{i=1}^{Q} \left(k_a B_{r,i}\right)^2 \boldsymbol{u}_i \qquad (15)$$

where $\boldsymbol{u}_i$ is the radial unit direction vector of tooth i, k_a is the coefficient which implies how much flux is entering into the airgap from the teeth, i.e. it describes the flux leakage, Q is the number of total slots and B_r is the radial flux density as measured by the search coil through time-integration of the induced voltage. The same measurement and calculation procedure have been repeated for different additional winding voltages, while the main winding of the motor is supplied with the 225 V. The computed and measured forces are presented in Fig. 11 [14]. It is worth mentioning that the force measurements have been conducted deliberately at no-load condition. The shaft is avoided being coupled to another machine which has bearing as it can lead to erroneous force estimation. Moreover, at loaded condition, the tangential component of the flux density cannot be neglected, however, its impact on the force computation is negligible. At rated operational point, the force computation using (15) can lead to an error of 3.83% for neglecting the B_{tan} component.
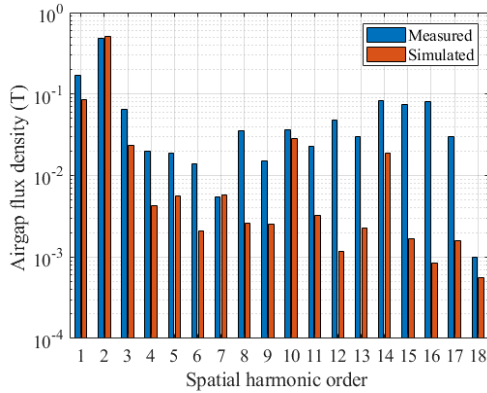

Fig. 10. Simulated and measured airgap flux density harmonics of the prototype machine at no load with additional winding energised.
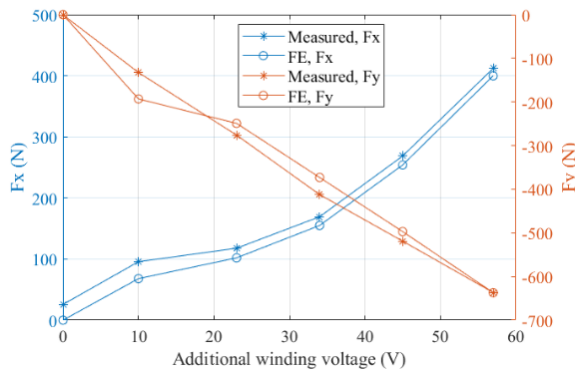

Fig. 11. Comparison of the forces measured with the search coil method and the simulated ones under different additional winding voltages [14].

It can be observed that the forces feature almost linear dependency on the additional winding voltage, especially the y-axis force. Since the machine is operated without any control, the force has increased in both directions of the machine. The measured and simulated forces match quite closely, however, between 0 and 20 V additional winding voltage there is a difference in the simulated and measured forces. This difference is attributed to the inherent eccentricity of the rotor. As the rotor position calibration has some inaccuracy, it leads to a slight eccentricity. The Fourier analysis of the simulated and measured force is then performed for the operation point corresponding to the additional winding terminal voltage of 57 V with the main winding voltage still at 225 V. These results are presented in Fig. 12, without the DC component of the forces for clarity of representation. The Fourier analysis of the measured forces shows high noises, especially in the lower temporal frequency region. The existence of the AMB induces additional harmonic in the search coil due to two reasons- 1. Electromagnetic coupling of the AMB and the motor, 2. The rotor is not perfectly centred but has a small static eccentricity due to the rotor calibration error which is quite common in this kind of measurement setup and very hard to overcome. These issues explain, to a large extent, the differences between the modelling and simulation. However, the overall force measurement including harmonics has been found more accurate and less noisy using search coil than measuring directly from the AMB. Moreover, the slot harmonics in the measured forces at 900 Hz can be noticed clearly in Fig 12.
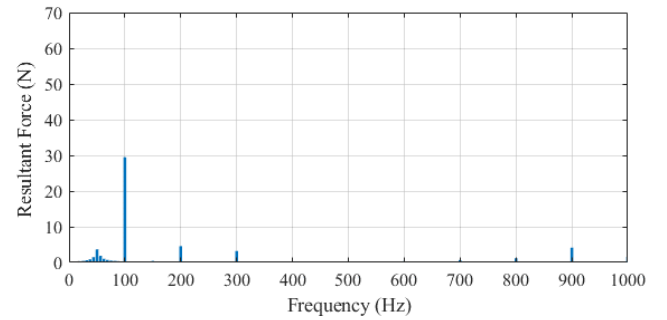
(a)
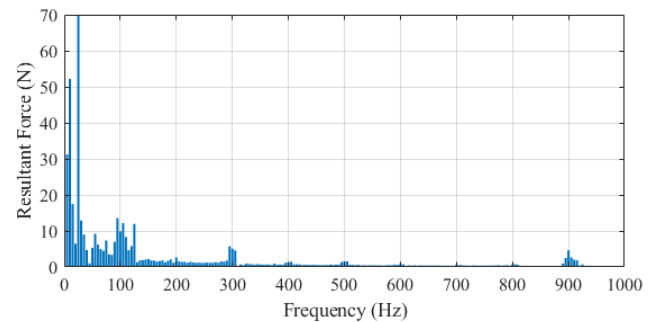
(b)

Fig. 12. Fourier analysis of the resultant y-axis force (without the dc component) for (a) FE computation and (b) Prototype measurement with the search coil method.

V. Conclusion

The primary motivation to express the electromagnetic forces as a function of spatial harmonics is to understand which spatial harmonics are helpful to produce the DC forces and which are the one that needs to be reduced. The presented methods can be used to analyze any bearingless machine as the model only requires the airgap flux density distribution in the airgap to compute the force harmonics. The proposed method gives a comprehensive structure to understand which specific pair of the flux density spatial harmonics produce force at a specific temporal frequency. To achieve this, the temporal harmonics are computed using the force decomposition method to segregate the force temporal harmonics from any given pair of the flux density spatial harmonics. To represent this, the concept of *SHI* is introduced. The advantage of the method is the easiness of understanding that how a pair of spatial harmonics behaves in the temporal spectrum. There are numerous literatures on torque ripple reduction by current harmonic injection which basically can be estimated by the behaviour of the spatial harmonics. A similar approach can be used if the force harmonic is needed to be compensated in real-time. Though in this paper the analysis is done using FE method, the presented force decomposition model can be also used for analytical models which makes it suitable in dynamic simulations. In addition, the torque harmonic is reduced by minimising certain spatial harmonic components by manipulating the airgap flux density distribution in the airgap with correct design choices. Similarly, the presented force harmonic model leverages the capability for the designer to choose the correct spatial flux distribution in the airgap to maximise the design objective.

It can be understood that some *SHI*s have dominant temporal footprint at 0 Hz, which means those spatial harmonics will produce mainly DC levitation force. Again, there are also some *SHI*, which have dominant temporal footprint in non-zero frequencies. This means that there are certain spatial harmonics, which will mainly produce force ripples. Therefore, this detail spatial harmonic information can be extracted from an initial design of a BSynRM with a time-stepping simulation and design objective can be chosen accordingly.

In this paper, we presented a force model and its usage in a novel way to compute the electromagnetic forces. The model is applied for the analysis of a BSynRM. The detailed analysis of the flux density harmonics provides an elaborate understanding on which harmonic component of the flux density is responsible for which force harmonic of the BSynRM. A novel harmonic indexing (*SHI*) method is presented to identify the spatial flux density harmonics responsible for different time harmonics of the forces.

Acknowledgment

References

[1] A. Chiba, T. Deido, T. Fukao and M. Rahman, "An analysis of bearingless AC motors," IEEE Trans. Ener. Convers., vol. 9, no. 1, pp. 61-68, March 1994.

[2] T. Reichert, T. Nussbaumer and J. W. Kolar, "Bearingless 300 W pmsm for bioreactor mixing," IEEE Trans. Indus. Electr., vol. 59, no. 3, pp. 1376-1388, March 2012.

[3] W. Amrhein, S. Silber and K. Nenninger, "Levitation forces in bearingless permanent magnet motors," IEEE Trans. Magn., vol. 35, no. 5, pp. 4052-4054, September 1999.

[4] J. Asama, M. Amada, N. Tanabe, N. Miyamoto, A. Chiba, S. Iwasaki, M. Takemoto, T. Fukao and M. A. Rahman, "Evaluation of a Bearingless PM Motor With Wide Magnetic Gaps," IEEE Trans. Ener. Convers., vol. 25, no. 4, pp. 957-963, March 2010.

[5] V. Mukherjee, A. Belahcen, M. Hinkkanen, "Active Magnetic Bearing Calibration to Compute Levitation Force in a Bearingless Synchronous Reluctance Motor Drive," in Closing Conference of the Project-Doctoral School of Energy and Geotechnology II, Pärnu, 2016.

[6] X. Cao, J. Zhou, C. Liu, and Z. Deng, "Advanced Control Method for a Single-Winding Bearingless Switched Reluctance Motor to Reduce Torque Ripple and Radial Displacement," IEEE Trans. Ener. Convers., vol. 32, no. 4, pp. 1533-1543, March 2017.

[7] B. Lapôtre, N. Takorabet, F. Meibody-Tabar, J. Fontchastagner, R. Lateb and J. D. Silva, "New Model of Radial Force Determination in Bearingless Motor," IEEE Trans. Magn., vol. 51, no. 3, pp. 1-4, March 2015.

[8] J. Aasama, T. Oiwa and A. Chiba, "Radial force investigation of a bearingless PM motor considering spatial harmonics of magnetic flux distribution," in 19th Int. Conf. Elec. Mach. Sys., Chiba, 2016, pp. 1-5.

[9] J. Martinez, A. Belahcen and A. Arkkio, "Combined FE and two dimensional spectral analysis of broken cage faults in induction motors," in IECON, 39th Annual Conf. IEEE Indus. Elect. Society, Vienna, 2013, pp. 2674-2679.

[10] R. Nertens, U. Pahner, K. Hameyer, R. Belmans and R. De Weerdt, "Force calculation based on a local solution of Laplace's equation," IEEE Trans. on Magn., vol. 33, no. 2, pp. 1216-1218, Mar 1997.

[11] J. L. Coulomb, "A methodology for the determination of global electromechanical quantities from a finite element analysis and its application to the evaluation of magnetic forces, torques and stiffness," IEEE Trans. Magn., vol. 19, no. 6, pp. 2514-2519, Nov 1983.

[12] A. Arkkio, "Analysis of induction motors based on the numerical solution of the magnetic field and circuit equations," Ph.D. dissertation, Helsinki Univ. of Technology, Espoo, Finland, 1987.

[13] A. Belahcen, V. Mukherjee, M. F. Far, P. Rasilo and M. Hinkkanen, "Coupled field and space-vector equations of bearingless synchronous reluctance machine," *XXII International Conference on Electrical Machines (ICEM)*, Lausanne, pp. 2581-2587, 2016.

[14] A. Belahcen, V. Mukherjee, F. Martin, P. Rasilo, "Computation of Hysteresis Torque and Losses in a Bearingless Synchronous Reluctance Machine," *IEEE Trans. Magn.*, volume 54, issue 3, pages 1-4, March 2018.

[15] V. Mukherjee, P. Rasilo, F. Martin and A. Belahcen, "Effect of Magnetic Forces and Magnetostriction on the Stator Vibrations of a Bearingless Synchronous Reluctance Motor," *IEEE Trans. Magn.*, vol. 55, no. 6, pp. 1-4, June 2019.